Supplementary Information

Quantifying Energy Transfer to Organic Dyes through Self-Trapped Excitonic and Dopant-Mediated Emission in $Cs_2NaBiCl_6$ Lead-Free Double Perovskite Nanocrystals

Kiran Hiremath, Bhakti Kulkarni, Anoopa Thomas, P. Muthu Austeria, R. Geetha Balakrishna*

Centre for Nano and Material Sciences, Jain (Deemed-to-be University), Bangalore-562112, Karnataka, India

*Corresponding author e-mail: br.geetha@jainuniversity.ac.in

1. Experimental Section

1.1 Materials and Chemicals:

Cesium carbonate (Cs_2CO_3, TCI), sodium acetate (NaOAc, Fisher Scientific), bismuth (III) acetate ($Bi(OAc)_3$, TCI), silver acetate (AgOAc, Sigma Aldrich), manganese (II) acetate dihydrate ($Mn(OAc)_2.2H_2O$, Sigma Aldrich), oleic acid (OA, 65%, SRL), oleylamine (OLA, pure 95%, SRL), 1-octadecene (ODE, technical grade, 90% Sigma Aldrich), n-hexane (Rankem), hydrochloric acid (HCl ≥ 35.40 %, Rankem). All chemicals were used without further purification.

1.2 Synthesis of Oleylammonium Chloride (OAm-Cl):

OAm-Cl was synthesized through a simple acid-base reaction approach. In brief, 6 mL of oleylamine (OLA) was heated to 120°C under vacuum for 40 minutes to remove any residual moisture and volatile impurities in a two-necked round bottom flask. The system was then switched to a nitrogen atmosphere, and 1 mL of concentrated HCl was slowly injected into the reaction mixture under continuous stirring. The solution was maintained at 120°C for an additional 30 minutes, allowing complete protonation of OLA to form oleylammonium chloride (OAm-Cl). This solution acts as a halide source and is preheated to 120°C before being injected during the perovskite synthesis.

1.3 Synthesis of Lead-free Double Perovskite $Cs_2NaBiCl_6$ (CNBC) NCs:

The lead-free double perovskite (DP) $Cs_2NaBiCl_6$ (CNBC) nanocrystals (NCs) were synthesized using a modified hot-injection method. In brief, 0.1 mmol of cesium carbonate (Cs_2CO_3), 0.1 mmol of bismuth (III) acetate ($Bi(OAc)_3$), and 0.1 mmol of sodium acetate (NaOAc) were combined with 6 mL of anhydrous 1-octadecene (ODE), 1.25 mL of oleic acid (OA), and 0.33 mL of oleylamine (OLA) in a three-necked round-bottom flask. The reaction mixture was then degassed at 120°C under vacuum for 1 hour to remove any residual moisture and volatile impurities. Later it was switched to a nitrogen atmosphere, and the temperature was raised to 200°C. Once a homogeneous temperature is achieved, 2.0 mL of preheated oleylammonium chloride (OAm-Cl) solution was swiftly injected into the mixture, initiating rapid nucleation and growth of the nanocrystals. After 10 seconds, the reaction was immediately quenched using an ice bath to arrest further growth. The resultant crude product was initially purified by centrifugation at 2,000 rpm for 3 minutes, allowing the removal of unreacted precursors and bulk byproducts. The collected supernatant was then washed with 10 mL of n-hexane and further purified by centrifugation at 12,000 rpm for 10 minutes. The final precipitate was redispersed in 5 mL of n-hexane for storage and subsequent characterization.[1]

1.4 Synthesis of Ag^+/Mn^{2+} doped Lead-free Double Perovskite $Cs_2NaBiCl_6$ (CNBC) NCs:

The synthesis of doped $Cs_2NaBiCl_6$ (CNBC) nanocrystals (NCs) was carried out following the same established protocol as for the undoped counterpart. However, the stoichiometric ratio of the host material was adjusted to accommodate the incorporation of dopant ions. In short, for Ag^+ doping, silver acetate (AgOAc) was used as the dopant precursor. The substitution of Na^+ with Ag^+ was controlled by varying the molar ratio of Na:Ag in the $Cs_2Na_{(1-x)}Ag_xBiCl_6$ composition, where x (0.04,0.08,0.12,0.16,0.20) was systematically varied to achieve different doping levels. For Mn^{2+} doping, manganese (II) acetate ($Mn(OAc)_2$) was used as the dopant precursor. In this case, both Na^+ and Bi^{3+} were partially substituted by Mn^{2+}, leading to the formation of $Cs_2Na_{(1-y)}Bi_{(1-y)}Mn_{2y}Cl_6$. The doping concentration was carefully controlled by selecting appropriate values of y (0.001, 0.003, 0.005, 0.007, 0.009). The reaction condition and the purification process were the same which was followed for the pristine CNBC synthesis.

2. Instrumentation:

2.1 Powder X-ray Diffraction: Powder XRD measurements were carried out using a Rigaku Ultima IV X-ray diffractometer, equipped with a Cu Kα radiation source (λ = 1.5406 Å) operated at 40 kV and 40 mA. The samples were drop-casted over a glass cover-slip. Data

were collected in θ–2θ geometry over a typical angular range of 5° to 60° (2θ) with a step size of 0.02° and a scan rate suitable for high-resolution analysis.

2.2. Transmission Electron Microscopy (TEM): TEM analysis was carried out using a Thermo Fisher Talos F200 S operated at an accelerating voltage of 200 kV, equipped with a field emission gun (FEG) and a 4K × 4K CMOS camera for high-resolution imaging.

2.3 UV-Vis Absorption Spectroscopy: UV-Vis absorption spectra were recorded using a Shimadzu UV-1800 double-beam spectrophotometer. The instrument features a wavelength range of 190–1100 nm, with a spectral bandwidth of 1 nm, ensuring high-resolution measurements. All measurements were conducted using quartz cuvettes with a 1 cm path length, and baseline correction was applied using a solvent blank. The system is equipped with a deuterium and tungsten-halogen lamp combination for continuous spectral coverage across the UV and visible regions. Data were acquired with UVProbe software, enabling precise spectral analysis and absorbance quantification.

2.4 Photoluminescence, Photoluminescence quantum yield (PLQY) and Time resolved Photoluminescence Spectroscopy: All steady-state, PLQY and time-resolved photoluminescence (PL) measurements were performed using an Edinburgh Instruments FLS 920 Fluorescence Spectrometer. The instrument is equipped with a 450 W xenon arc lamp for steady-state excitation, integrating sphere for absolute PLQY and a microsecond pulsed xenon flashlamp (μF2) for lifetime measurements. The system includes a double monochromator setup for both excitation and emission paths, ensuring high spectral resolution and reduced stray light. Emission was collected using a photomultiplier tube (PMT) detector (R928P, Hamamatsu), and data acquisition was carried out with time-correlated single-photon counting (TCSPC) for nanosecond–microsecond lifetime analysis. The instrument offers a wavelength range of 200–1700 nm and a temporal resolution down to 200 ps. All measurements were conducted at room temperature in quartz cuvettes with a path length of 1 cm.

2.5 X-ray Photoelectron Spectroscopy (XPS): XPS analysis was performed using a Thermo Fisher Scientific X-ray Photoelectron Spectrometer equipped with an analyzer with 180° double focusing hemispherical analyzer with 128-channel detector, monochromatic Al Kα source micro focused, ion gun energy range of 100 - 4000 eV. The system operates under ultra-high vacuum (UHV) conditions and provides surface-sensitive elemental and chemical state information. Data acquisition and peak fitting were carried out using Thermo Avantage software.

2.6 Electron Paramagnetic Resonance (EPR) Spectroscopy: EPR measurements were carried out using a JEOL JES-X320 spectrometer. The system operates in the X-band (~9.5 GHz) and is equipped with a high-sensitivity resonator for detecting unpaired electron species. All spectra were recorded at room temperature, and the instrument parameters were optimized to ensure accurate signal detection and resolution.

2.7 Density Functional Theory (DFT) Calculation: DFT calculations were performed using the Perdew-Burke-Ernzerhof (PBE)[2] function within the generalized gradient approximation (GGA)[3], as implemented in the VASP package.[4, 5] A plane wave cut-off energy of 450 eV was used for geometry optimization. All structures were optimized in the same level of theory with k-point sampling of 4x4x4 with gamma point. The structures were fully relaxed until energy and forces are converged to 10^{-5} eV and 0.01 eV $Å^{-1}$. Local Density Approximation + Hubbard (U) (LDA+U) is used for all calculations for accurate description of the systems. Density of states (DOS) were calculated using same level of theory.

3. Double Reciprocal Analysis of PL Quenching Data and K_{app}:

Double reciprocal analysis of fluorescence quenching data is an extension of the Benesi-Hildebrand method for estimating binding constants using absorbance data.[6, 7] This approach has been applied to estimate the association between numerous surface-adsorbed molecules and nanoparticles.[8]

The analysis is based on two assumptions, firstly there exists an equilibrium between the quencher (Q) and the emissive species (E), where they transition between their unbound and bound states. This equilibrium is controlled by an apparent association constant, denoted as K_{app}.

$$Q + E \longleftrightarrow [Q\text{----}E] \quad (1)$$

The second assumption considered was fluorescence intensity (ϕ) is directly proportional to the fluorescence quantum yield (ϕ_{PLQY}). This assumption holds here since there are no complicated factors such as self-absorption or significant scattering.[9]

Under these assumptions, the observed fluorescence intensity (ϕ_{obs}) is related to the fluorescence intensity of unbound(Φ_0) and bound (Φ') species through a degree of association α.

$$\phi_{obs} = (1 - \propto)\phi_o + \propto \phi^1 \quad (2)$$

Rearranged to

$$\phi_o - \phi_{obs} = \propto \left(\phi_o - \phi^1\right) \tag{3}$$

Typically for nanoparticle emission quenching by the molecules, the quencher concentration tends to be much higher than the nanoparticle concentration. So, for a relatively higher concentration of quencher, we can write α as:

$$\propto = \frac{K_{app}[Q]}{1 + K_{app}[Q]}$$

Substituting $\propto$ into equation 3:

$$\phi_o - \phi_{obs} = \frac{K_{app}[Q]}{1 + K_{app}[Q]} \times (\phi_o - \phi^1)$$

which can be rearranged into the form y = mx + b,

$$\frac{1}{(\phi_o - \phi_{obs})} = \frac{1}{(\phi_o - \phi^1)} + \frac{1}{\left(\phi_o - \phi^1\right)K_{app}[Q]}$$

If the quencher and emitter form an equilibrium with complex as denoted in equation 1 a linear relation can be established between $\frac{1}{(\phi_o - \phi_{obs})}$ and $\frac{1}{[Q]}$. The apparent association constant (K_{app}) can be calculated from the slope and intercept of this linear plot.

4. Supporting figures:

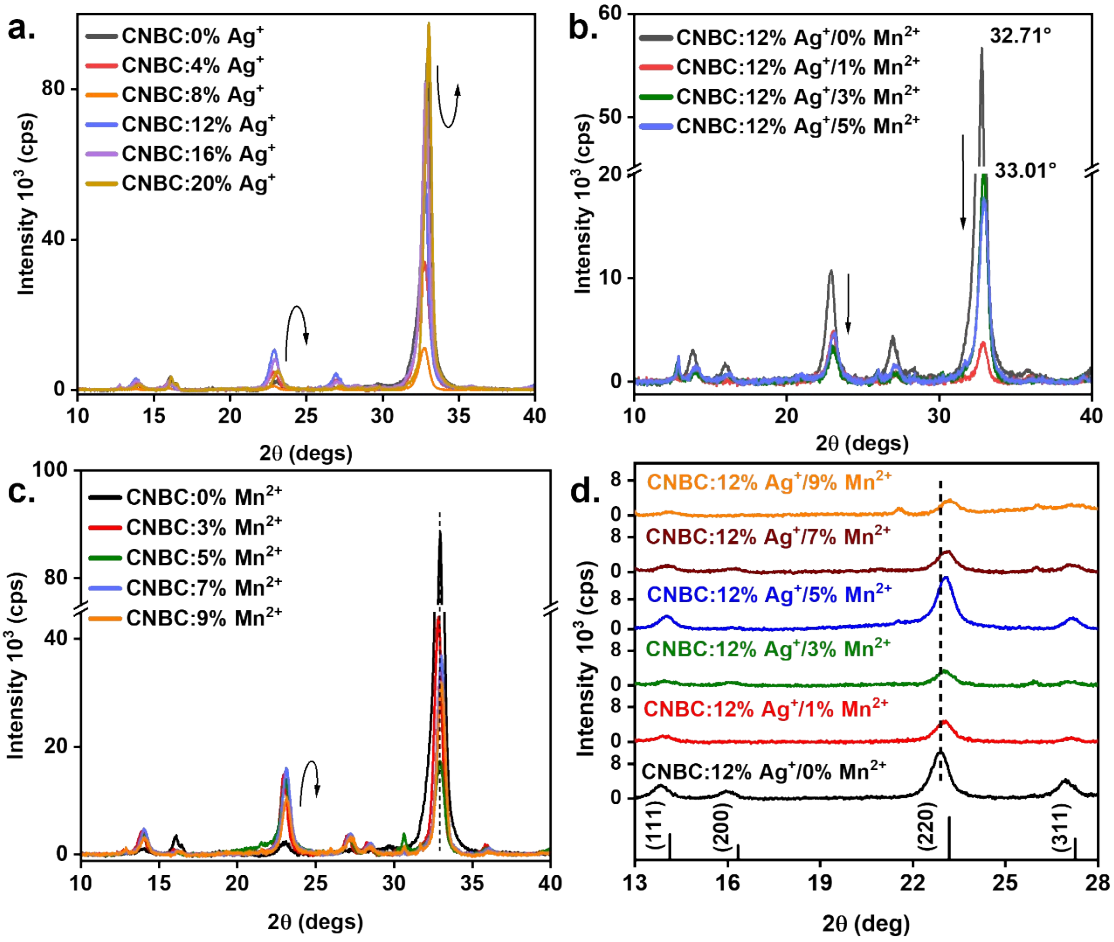

Figure S1: PXRD patterns of a) Ag^{+}-doped, b) Ag^{+}/Mn^{2+} co-doped CNBC NCs, c) Mn^{2+}-doped CNBC NCs, and d) enlarged diffraction patterns of Mn^{2+} doped CNBC NCs.

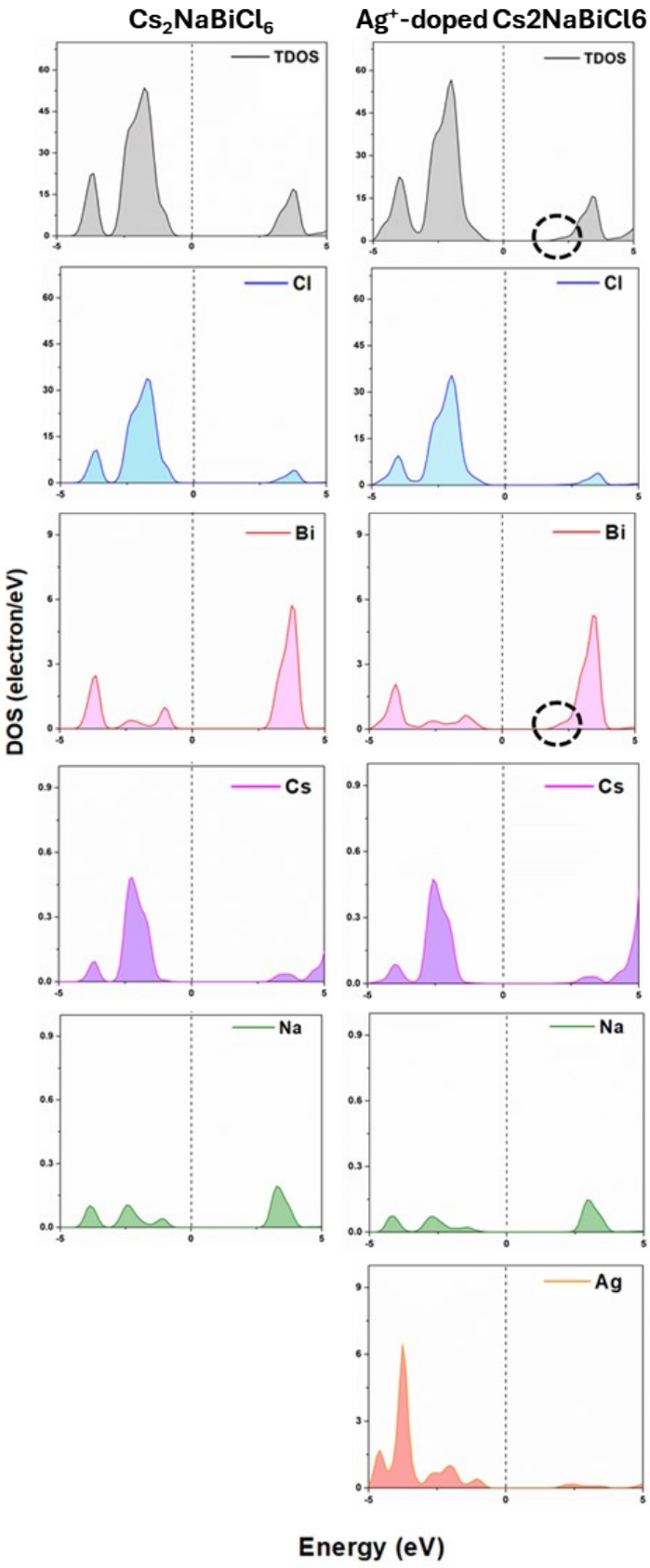

Figure S2: The total and partial DOS for $Cs_2NaBiCl_6$ and Ag-doped $Cs_2NaBiCl_6$.

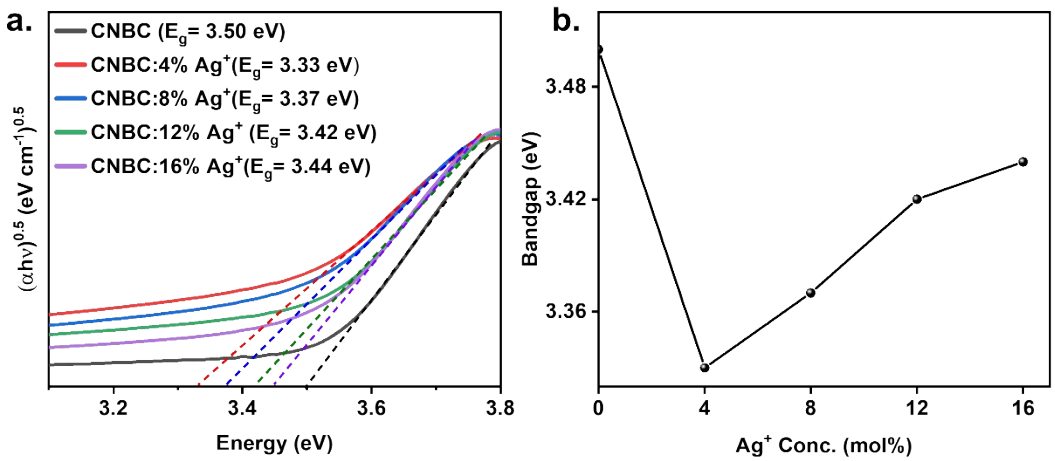

Figure S3: a) Tauc plot of Ag^+-doped CNBC NCs, b) Linear plot of Ag^+ concentration vs E_g.

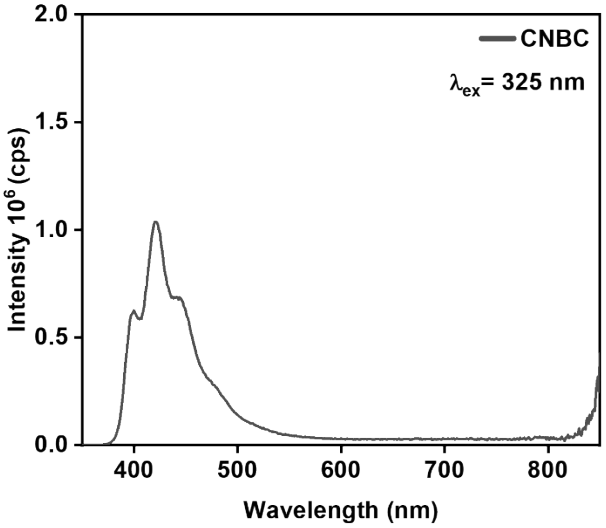

Figure S4: Emission spectra of undoped CNBC NCs at 325 nm excitation wavelength.

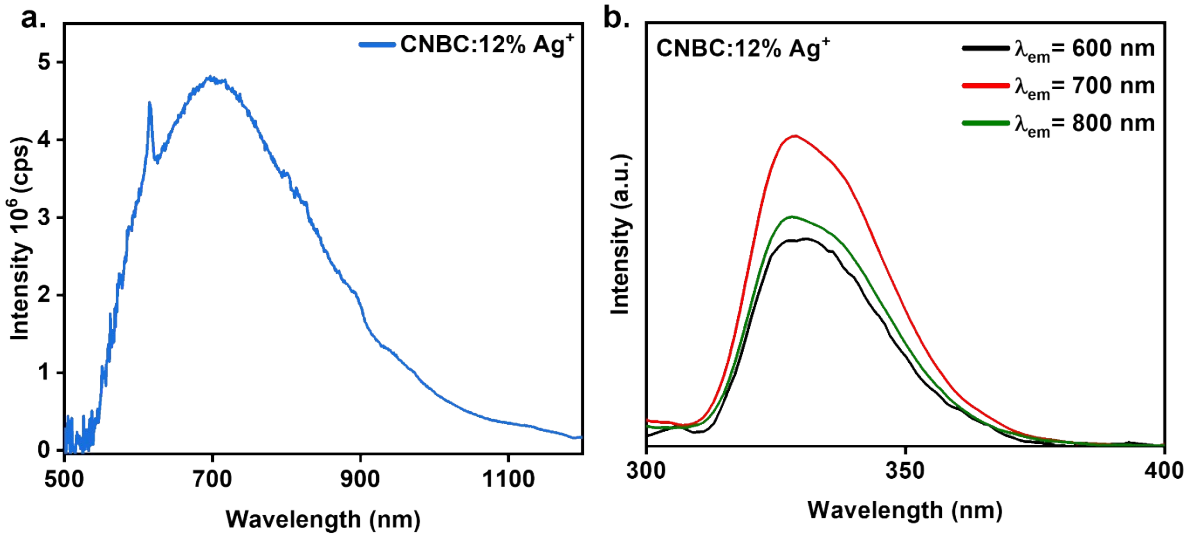

Figure S5: a) Photoluminescence (PL) emission spectra of Ag^{+}-doped CNBC NCs with 325 nm excitation wavelength, b) Photoluminescence excitation (PLE) spectra of Ag^{+}-doped CNBC NCs with emission fixed at different wavelengths.

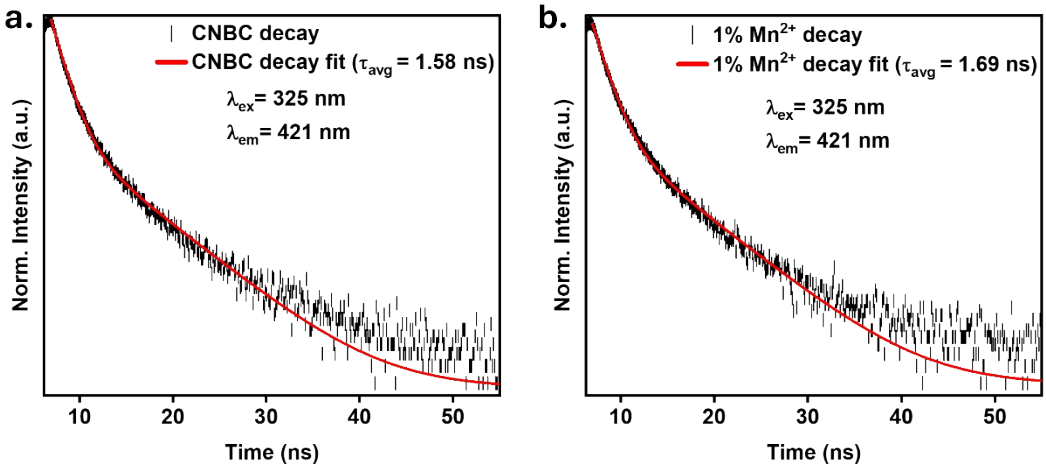

Figure S6: Time resolved decay curves of a) undoped CNBC NCs, and b) CNBC:5% Mn^{2+} at fixed emission wavelength at 421 nm and excitation wavelength 325 nm.

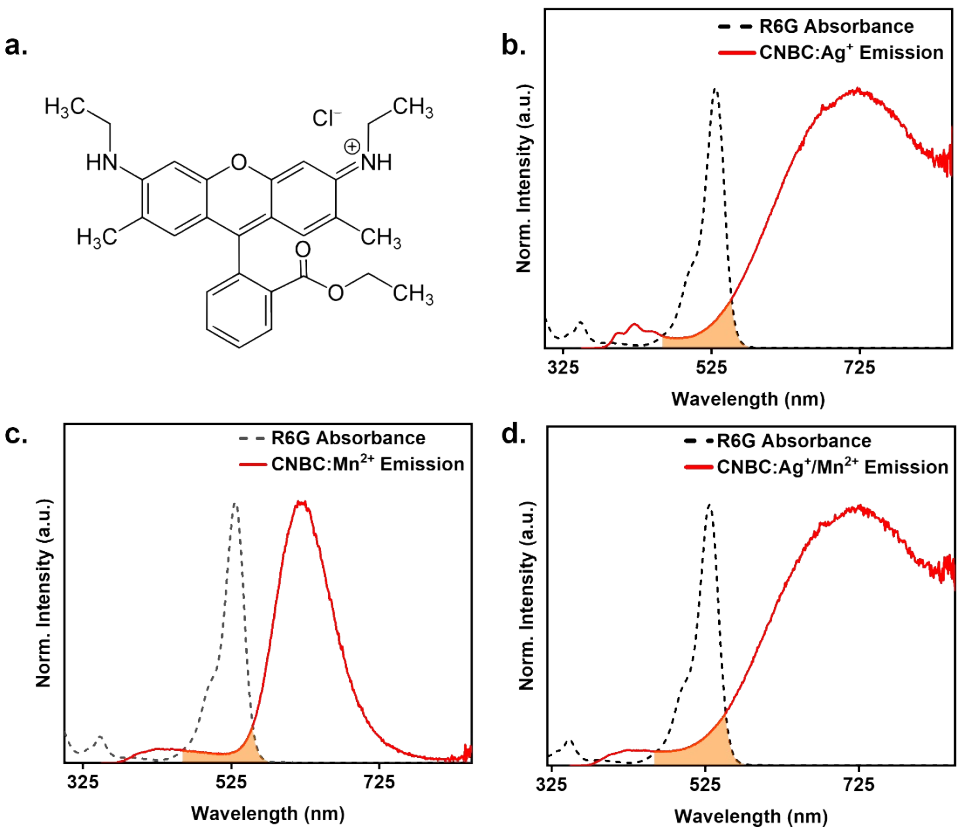

Figure S7: a) Structure of rhodamine 6G (R6G) dye, spectral overlap of PL and UV-Vis absorption spectra of b) Ag^{+}-doped, c) Mn^{2+}-doped and d) Ag^{+}/Mn^{2+} co-doped CNBC NCs and R6G dye respectively.

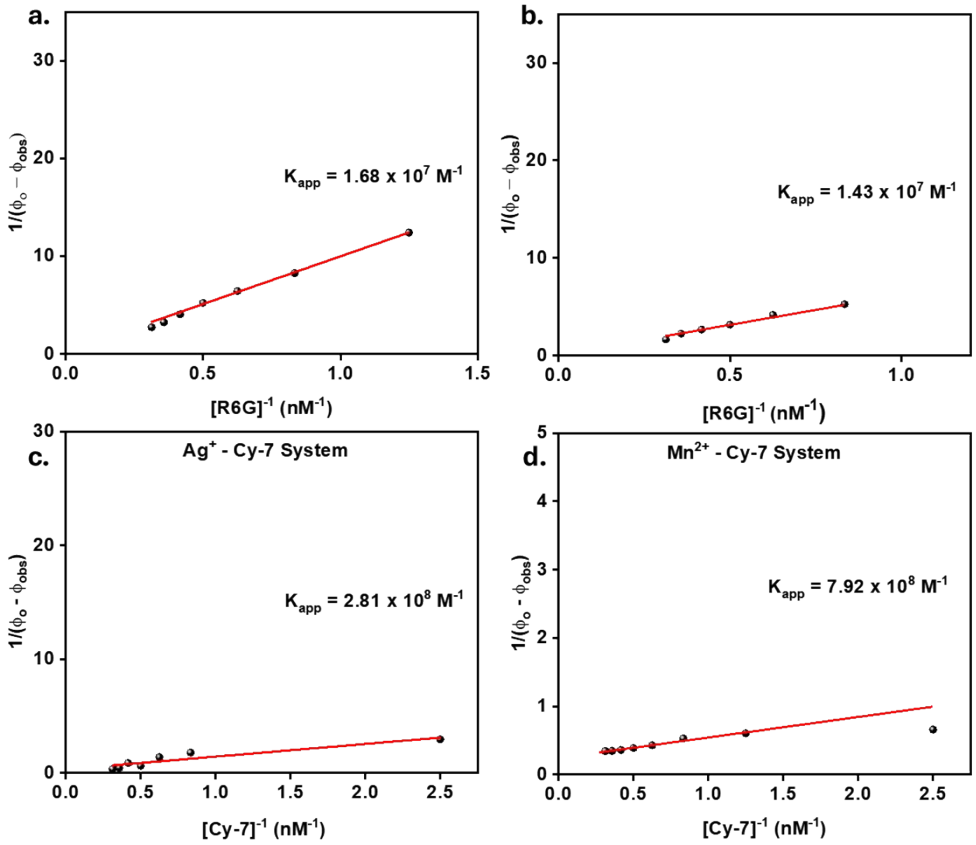

Figure S8: Double reciprocal PL quenching (Benesi-Hildebrand) plot of a) Ag^+-doped, b) Ag^+/Mn^{2+} co-doped CNBC NCs paired with R6G dye molecules, c) Ag^+-doped and Mn^{2+}-doped CNBC NCs paired with Cy-7 dye molecules.

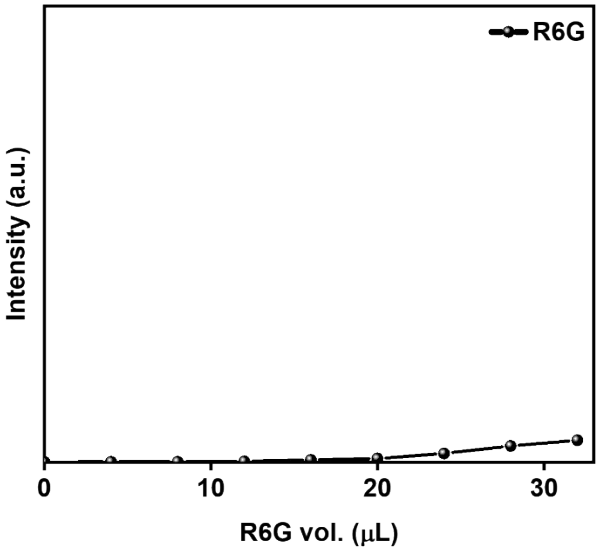

Figure S9: Control experiment showing PL intensity with increasing amount of R6G in the system.

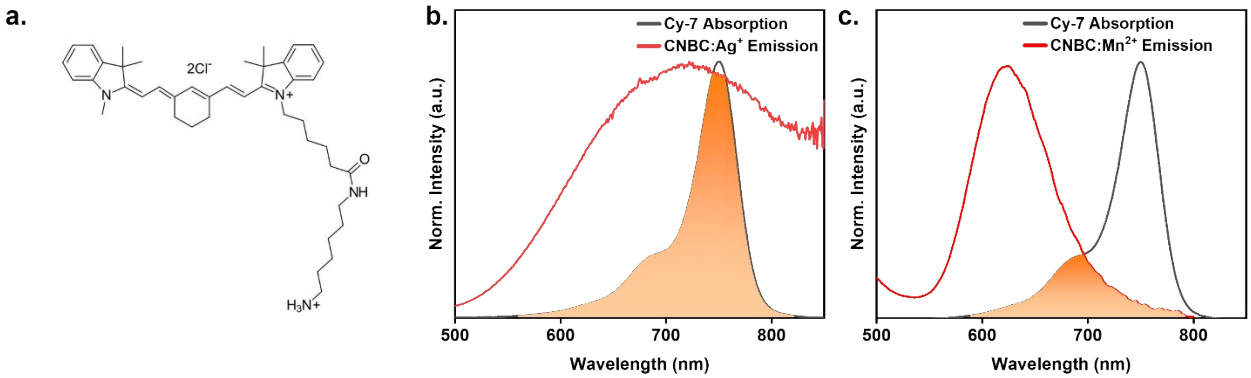

Figure S10: a) Structure of cyanine 7-amine (Cy-7) dye, spectral overlap of PL and UV-Vis absorption spectra of a) Ag^{+}-doped, and b) Mn^{2+}-doped CNBC NCs and Cy7 dye respectively.

Table S1: Atomic ratio of the undoped and doped NCs calculated using XPS data.

Sample	**Atomic composition by XPS (at. %)**					
	Cs^{+}	**Na^{+}**	**Bi^{3+}**	**Cl^{-}**	**Mn^{2+}**	**Ag^{+}**
Undoped CNBC	18.46	9.83	11.67	60	-	-
12% Ag^{+}-doped CNBC	17.72	8.43	9.26	60	-	4.20
5% Mn^{2+}-doped CNBC	19.68	8.46	5.51	60	5.15	-

Table S2: Inductively coupled-plasma mass spectroscopy (ICP-MS) elemental analysis of the doped CNBC NCs.

Sample	**Element**	**Species**	**Expected (%)**	**Measured (%)**
12% Ag^{+}-doped CNBC	Ag/(Na+Ag)	Ag^{+}	12.0	4.23
5% Mn^{2+}-doped CNBC	Mn/(Na+Bi+Mn)	Mn^{2+}	5.0	1.89
12% Ag^{+}/1% Mn^{2+} co-doped CNBC	Ag/(Na+Ag)	Ag^{+}	12.0	6.51
	Mn/(Na+Bi+Mn)	Mn^{2+}	1.0	1.32

Table S3: The absolute photoluminescence quantum yield (PLQY) of the doped NCs.

Sl. No.	Sample	PLQY (%)
1	4% Ag^{+}	4.7
2	12% Ag^{+}	5.25
3	16% Ag^{+}	2.9
4	1% Mn^{2+}	0.84
5	5% Mn^{2+}	0.99
6	7% Mn^{2+}	0.97
7	12% Ag^{+}/1% Mn^{2+}	2.83
8	12% Ag^{+}/5% Mn^{2+}	2.67
9	12% Ag^{+}/7% Mn^{2+}	2.35

Table S4: Peak contribution of Ag^{+}-doped CNBC NCs with increasing amount of Mn^{2+} concentration.

Sl. No.	Sample	Peak Intensity at 620 nm (Mn) (10^6 cps)	Peak Intensity at 720 nm (Ag) (10^6 cps)	Intensity ratio (Mn/Ag)
1	12% Ag^{+}/0% Mn^{2+}	4.2	6.0	0.70
2	12% Ag^{+}/1% Mn^{2+}	1.84	2.40	0.76
3	12% Ag^{+}/5% Mn^{2+}	1.36	1.74	0.78
4	12% Ag^{+}/7% Mn^{2+}	0.16	0.19	0.84

Table S5: The following table shows the decay parameters obtained for the respective samples at the indicated fixed emission wavelengths and an excitation wavelength of 325 nm.

Sample	Emission (λ_{em})	A1	A2	τ_1 (s)	τ_2 (s)	τ_{avg}
4% Ag^{+}	720 nm	6028.122	4705.737	3.55E-06	9.55E-06	6.18 μs

12% Ag^{+}		4773.344	5677.31	3.88E-06	9.69E-06	7.04 µs
16% Ag^{+}		4633.468	5751.608	3.94E-06	9.64E-06	7.09 µs
1% Mn^{2+}	620 nm	472.0667	1686.416	6.01E-03	1.37E-02	12.03 ms
5% Mn^{2+}		603.3705	2179.372	3.59E-03	1.36E-02	11.4 ms
7% Mn^{2+}		584.8806	1940.511	2.47E-03	1.28E-02	10.4 ms
12% Ag^{+}/1% Mn^{2+}	720 nm	7009.929	3685.038	2.86E-06	9.45E-06	5.13 µs
12% Ag^{+}/5% Mn^{2+}		7399.416	3317.745	2.81E-06	9.51E-06	4.89 µs
12% Ag^{+}/7% Mn^{2+}		7994.61	2789.177	2.60E-06	9.63E-06	4.42 µs

4. FRET calculations:

The efficiency of FRET depends on the degree of spectral overlap J(λ) between the donor's emission and the acceptor's absorption. To calculate this, we used the a|e spectral analysis tool (a|e - UV-Vis-IR Spectral Software 1.2, FluorTools, www.fluortools.com). Spectral overlap was evaluated for the emissions of our Ag^{+}-doped, Mn^{2+}-doped, and Ag^{+}/Mn^{2+} co-doped CNBC nanocrystals with the absorption spectrum of Rhodamine 6G and cyanine-7 amine dye in *n*-hexane. For this calculation, we considered a peak molar extinction coefficient of 116,000 $L.mol^{-1}.cm^{-1}$ and 199,000 $L.mol^{-1}.cm^{-1}$ for Rhodamine 6G and Cyanine-7 amine. The resulting spectral overlap values are summarized in the following **Table S6**.

Table S6: Spectral overlap calculated using a|e spectral analysis tool.

Donor-acceptor pair	**Overlap integral** ($nm^4M^{-1}cm^{-1}$)
Ag^{+}-doped CNBC - R6G	6.235×10^9
Mn^{2+}-doped CNBC - R6G	3.542×10^9
Ag^{+}/ Mn^{2+} co-doped CNBC - R6G	6.196×10^9
Ag^{+}-doped CNBC - Cy7	2.655×10^{11}
Mn^{2+}-doped CNBC - Cy7	3.314×10^{10}

Forster radius:

The Forster radius can be obtained using the following equation **(1)**:

$$R_0 = 0.221 \left(\frac{\kappa^2 \phi_D J(\lambda)}{n^4} \right)^{\frac{1}{6}} \quad \textbf{(1)}$$

Where, κ^2 is orientation factor (2/3 for freely rotating donor and acceptors), ϕ_D the donor photoluminescence quantum yield, $J(\lambda)$ the spectral overlap of the donor emission and acceptor absorption, and *n* is the refractive index.[10] The calculated R_0 values for the samples are summarised in the **Table S7** below.

Table S7: Forster radius (R_0) of the doped nanocrystals calculated using equation (1).

Donor-acceptor pair	**Forster radius R_0 (nm)**
Ag^+-doped CNBC - R6G	4.38
Mn^{2+}-doped CNBC - R6G	2.38
Ag^+/ Mn^{2+} co-doped CNBC - R6G	3.50
Ag^+-doped CNBC - Cy7	7.82
Mn^{2+}-doped CNBC - Cy7	3.30

Data analysis:

Although FRET treats donor and acceptor as point dipoles, the Wannier-Mott excitons in perovskites are extended objects and the energy transfer may require multipole treatment. In our work we have assumed that the luminescence occurs from multiple points within the NCs as shown in following **schematic**. The NCs are capped by ligands oleic acid and oleylamine which have an extended length of ~2.08 nm and ~2.0 nm respectively. When the dye molecule interacts with NCs capped with ligands there is formation of FRET pair (donor-acceptor). With a calculated average size of the nanocrystal (**9.49 nm**) and luminescence originating from different points as denoted in the schematic we calculated the FRET efficiency using the following equation **(2)**.[11, 12]

$$E = \frac{1}{\left(1 + \frac{R}{R_0}\right)^6} \quad \textbf{(2)}$$

Where, E is the FRET efficiency, R is the distance between the donor and acceptor, and R_0 the Forster radius. The summarized data is shown in the tabular column below.

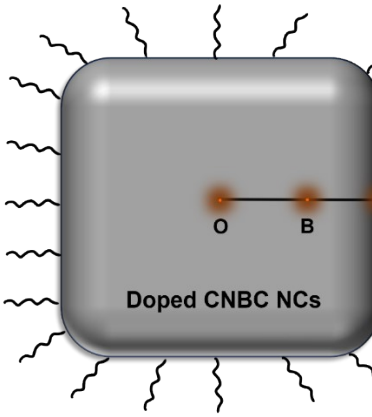

Mean size of the nanocrystal	9.49 nm
Average length of extended ligand (AD)	2.04 nm
AO	4.74 nm
AB	2.37 nm

Schematic representation of nanocrystal-dye FRET pair and their distance

Table S8: Calculated FRET efficiency based on different emission origins.

Sample	**Emission originates from point 'O'**		**Emission originates from point 'B'**		**Emission originates from point 'A'**	
	FRET Distance (nm) 'R'	**FRET Efficiency 'E'**	**FRET Distance (nm) 'R'**	**FRET Efficiency 'E'**	**FRET Distance (nm) 'R'**	**FRET Efficiency 'E'**
Ag^{+}-doped CNBC + R6G	6.78	6.8 %	4.41	49.0 %	2.04	98.99 %
Mn^{2+}-doped CNBC + R6G		0.77 %		9.36 %		92.01 %
Ag^{+}/Mn^{2+} co-doped CNBC + R6G		3.76 %		34.05 %		98.13 %
Ag^{+}-doped CNBC + Cy7		70.2 %		96.8 %		99.9 %

Mn^{2+}-doped CNBC + Cy7		6.77 %		48.97 %		98.9 %

References:

1. Mai, H., et al., *Synthesis of layered lead-free perovskite nanocrystals with precise size and shape control and their photocatalytic activity.* Journal of the American Chemical Society, 2023. **145**(31): p. 17337-17350.
2. Perdew, J.P., K. Burke, and M. Ernzerhof, *Generalized Gradient Approximation Made Simple.* Physical Review Letters, 1996. **77**(18): p. 3865-3868.
3. Kresse, G. and J. Hafner, *Ab initio molecular dynamics for liquid metals.* Physical Review B, 1993. **47**(1): p. 558-561.
4. Kresse, G. and J. Hafner, *Ab initio molecular-dynamics simulation of the liquid-metal--amorphous-semiconductor transition in germanium.* Physical Review B, 1994. **49**(20): p. 14251-14269.
5. Kresse, G. and D. Joubert, *From ultrasoft pseudopotentials to the projector augmented-wave method.* Physical Review B, 1999. **59**(3): p. 1758-1775.
6. Benesi, H.A. and J.H. Hildebrand, *A Spectrophotometric Investigation of the Interaction of Iodine with Aromatic Hydrocarbons.* Journal of the American Chemical Society, 1949. **71**(8): p. 2703-2707.
7. Kamat, P.V., *Photochemistry on nonreactive and reactive (semiconductor) surfaces.* Chemical Reviews, 1993. **93**(1): p. 267-300.
8. Kato, D., et al., *Synthesis, Structural and Photophysical Properties of Pentacene Alkanethiolate Monolayer-Protected Gold Nanoclusters and Nanorods: Supramolecular Intercalation and Photoinduced Electron Transfer with C60.* The Journal of Physical Chemistry C, 2017. **121**(16): p. 9043-9052.
9. Lakowicz, J.R., *Principles of fluorescence spectroscopy*. 2006: Springer.
10. Feld, L.G., et al., *Quantifying Förster Resonance Energy Transfer from Single Perovskite Quantum Dots to Organic Dyes.* ACS Nano, 2024. **18**(14): p. 9997-10007.
11. Cardullo, R.A., *Theoretical Principles and Practical Considerations for Fluorescence Resonance Energy Transfer Microscopy*, in *Methods in Cell Biology*. 2007, Academic Press. p. 479-494.
12. Anzola, M., et al., *Understanding Förster Energy Transfer through the Lens of Molecular Dynamics.* Journal of Chemical Theory and Computation, 2020. **16**(12): p. 7281-7288.